Ceramics International 48 (2022) 6835–6841

Contents lists available at ScienceDirect

Ceramics International

journal homepage: www.elsevier.com/locate/ceramint

A new chemresistive NO_2 sensing material: Hafnium diboride

Sikai Zhao [a,b,c,1], Yong Xia [a,b,d,1], Steven DelaCruz [a,b,1], Aifei Pan [a,b,d], Zhou Li [a,b], Yanbai Shen [c], Marcus A. Worsley [e], Carlo Carraro [a,b], Roya Maboudian [a,b,*]

[a] Department of Chemical and Biomolecular Engineering, University of California, Berkeley, CA, 94720, United States
[b] Berkeley Sensor & Actuator Center, University of California, Berkeley, CA, 94720, United States
[c] School of Resources and Civil Engineering, Northeastern University, Shenyang 110819, China
[d] School of Mechanical Engineering, Xi'an Jiaotong University, Xi'an, 710049, China
[e] Lawrence Livermore National Laboratory, Livermore, CA, 94551, United States

ARTICLE INFO

Keywords:
HfB_2
Metal diborides
Nanoparticles
NO_2
Gas sensing

ABSTRACT

While metal oxides and metal sulfides have been extensively studied for gas sensing applications, there are no extensive reports on gas sensing properties of metal diborides. Here, for the first time, we have investigated the conductometric gas sensing behavior of HfB_2 nanoparticles. The HfB_2 nanoparticles is synthesized via a sol-gel method and characterized using X-ray diffraction, field emission scanning electron microscopy, transmission electron microscopy, and X-ray photoelectron spectroscopy. The gas sensor is fabricated by drop casting the HfB_2 nanoparticles on interdigitated Ag/Pd electrodes. The sensor exhibited a promising NO_2 sensing performance at the operating temperature of 200 °C. Interestingly, it is found that resistance of the sensor decreases upon exposure to both oxidizing and reducing gases, which does not follow the gas sensing behaviors of the widely investigated metal oxides. In addition, the sensor response is minimally influenced by oxygen background concentration. These results highlight that HfB_2 nanoparticles exhibit very unique sensing characteristics.

1. Introduction

In 1962, Seiyama et al. proposed using the phenomenon of ZnO resistance change upon exposure to reducing gases for gas detection [1]. Since then, conductometric gas sensors have attracted great interest, have been extensively investigated and developed, and have become one of the most widely used devices for gas detection [2–4]. The basic working principle of conductometric gas sensors is based on the electrical conductivity change of the sensors upon exposure to the target gas due to the adsorption and reaction of the gas on the surface of the sensing material that is integrated into various solid-state sensors [5–7]. Thus, the properties of the gas sensing materials play a key role in determining the performance of such gas sensors, and the continued advancement of such gas sensors hinges on the development of the gas sensing materials.

Motivated by the pursuit of better sensing performance, researchers over the past few decades have extensively developed and studied various materials for conductometric gas sensing applications. These include metal oxides (e.g., ZnO, In_2O_3, WO_3, NiO, CuO) [8–13], metal sulfides (e.g., ZnS, PbS, WS_2) [14–16], metal-organic-frameworks (MOFs) [17], graphene [18,19], transition metal dichalcogenides (e.g., MoS_2, WSe_2) [20,21], conductive polymers [22,23], and MXenes [24,25]. However, to date, there is no experimental knowledge of the gas sensing properties of metal diborides.

Hafnium diboride (HfB_2), a typical metal diboride, is known as excellent ultra-high temperature ceramic and is characterized by good chemical stability, high melting point, and high strength [26]. It also possesses other qualities such as excellent oxidization resistance, high hardness, high ablation resistance, and is electrically conductive [27]. Owing to these unique properties, HfB_2 has been considered as an ideal candidate for applications that involve extreme conditions, such as neutron absorber in nuclear reactors, wear-resistant coating, plasma arc electrodes, and shielding for hypersonic vehicles [28]. Recent efforts have focused on applications of HfB_2 in solar energy absorbers and electrocatalysts [29]. Via theoretical calculations, Xiong et al. [30] predicted the presence of Dirac cone in two-dimensional (2D) HfB_2, as well as the good stability, high carrier mobility, and excellent electronic transport properties. These indicate that low-dimensional HfB_2 could be

* Corresponding author. Department of Chemical and Biomolecular Engineering, University of California, Berkeley, CA, 94720, United States.
E-mail address: maboudia@berkeley.edu (R. Maboudian).
[1] The authors contributed equally to this work and should be considered as co-first authors.

https://doi.org/10.1016/j.ceramint.2021.11.235
Received 8 September 2021; Received in revised form 19 November 2021; Accepted 23 November 2021
Available online 25 November 2021

a promising material in nanoelectronics and sensing devices, especially in those expected to work in harsh environments. Although the application space of HfB_2 is expanding, experimental studies on its gas sensing properties have not yet been reported.

Here, we present what we believe is the first report on the conductometric gas sensing behavior of HfB_2 nanoparticles. The HfB_2 nanoparticles was prepared by a sol-gel route followed by high-temperature annealing processes, and the sensor was fabricated by coating the prepared HfB_2 nanoparticles on an interdigitated Ag/Pd electrode. The sensor showed promising NO_2 sensing properties at the operating temperature of 200 °C. The results indicate that HfB_2 may provide a new choice in the material library for the fabrication of next-generation gas sensors.

2. Experimental

2.1. Material synthesis

The preparation method of HfB_2 nanoparticles was detailed in our previous report [28]. Briefly, boron nanoparticles (Specialty Materials, Inc.) with an average size of 30 nm were dispersed in ethanol to form the ethanolic boron suspension. Hafnium tetrachloride (Sigma-Aldrich 98%) and deionized water with the molar ratio of $H_2O/Hf/B = 34/1/10$ were added to the suspension and then chilled to 0 °C. The propylene oxide (Sigma-Aldrich 99%, PO) with the PO/Hf molar ratio of 9:1 was added to the mixture while stirring. Then, the wet gel was collected and washed with acetone followed by an ambient drying process. The dried gel was borothermally reduced in a graphite furnace at 1100 °C under a helium gas flow (Eq. (1)). Finally, to evaporate the remaining B_2O_3 and obtain high purity HfB_2, a second annealing process was subsequently conducted at 1600 °C (Eq. (2)).

$$3HfO_2(s) + 10B(s) \rightarrow 3HfB_2(s) + 2B_2O_3(l) \quad (1)$$

$$2B_2O_3(l) \rightarrow 2B_2O_3(g) \quad (2)$$

2.2. Material characterizations

The X-Ray diffraction (XRD) pattern was recorded on a powder diffractometer (Rigaku Miniflex) with Cu K_α radiation ($\lambda = 0.15406$ nm) for phase structure analysis. The morphology and microstructure were studied by using field emission scanning electron microscopy (FESEM, Zeiss Ultra 55) and transmission electron microscopy (TEM, JEM-2100), with the operating voltages of 5 and 200 kV, respectively. The surface chemistry and composition were investigated by X-Ray photoelectron microscopy (XPS, Thermo Scientific Escalab 250Xi) using monochromatic Al K_α source.

2.3. Gas sensor fabrication and gas sensing measurements

An interdigitated Ag/Pd electrode was used as the sensing electrode in this study, shown in Fig. S1. Seven pairs of 7 μm thick interdigitated Ag/Pd lines are deposited on a 635 μm thick alumina substrate with width and length of 7 and 13.4 μm, respectively. The Ag/Pd line width is 210 μm and the spacing between two adjacent lines is 190 μm. The prepared HfB_2 nanoparticles is homogeneously dispersed in ethanol and then drop-casted on the Ag/Pd electrode using a pipette to form the sensing layer.

Fig. S2 shows the gas sensing test apparatus. The gas cylinders are individually connected to mass flow controllers (MFC, Bronkhorst) that control the mass flow rates of the gases delivered to the chamber. The target gas is diluted with pre-dried house air or N_2 to obtain a specific concentration of the target gas and then delivered to the test chamber with a total flow rate of 300 sccm. All the MFCs in the gas delivery system are controlled by a LabView program. The test chamber is made out of stainless steel and is around 13 cm^3 in volume. The interdigitated Ag/Pd electrode-based sensor is posited on a circular miniature heater with a diameter of 5 mm. The temperature of the heater is controlled by an external DC power supply (Sorensen, DCS2600-1.7E) and measured by a thermocouple connected to backside of the heater. The resistance of the sensor is measured using a Keithley 2602 source meter. A Java-based software suit, Zephyr, is used to record the real-time data from the gas delivery system and source meter.

The sensor response is defined as $(R_a - R_g)/R_a$, where R_a and R_g are the resistance of the sensor in air and in analyte gases, respectively. The response and recovery times are defined as the times for the sensor to achieve 90% of the full resistance once the target gas concentration changes, as shown in Fig. S3. The gases reported in this study include NO_2 (Praxair, 21.8 ppm in N_2), ethanol (Airgas, 978 ppm in N_2), formaldehyde (Praxair, 22.1 ppm in N_2), acetone (Airgas, 409 ppm in N_2), carbon dioxide (Airgas, 20,200 ppm in N_2) and ammonia (Praxair, 9.39 ppm in N_2).

3. Results and discussions

3.1. Material characterizations

XRD pattern of the prepared HfB_2 nanoparticles is shown in Fig. 1. The observed distinct peaks match well with the characteristic peaks of hexagonal HfB_2 according to ICDD PDF card #38–1398, and the three strong peaks at 25.61°, 32.89°, and 42.13° correspond to (001), (100), and (101) crystal planes, respectively. The sharp shape of these diffraction peaks indicates the high crystallinity of the prepared HfB_2 nanoparticles. However, two faint peaks at the 2θ angles of around 35.00° and 38.00° are also found in the pattern, which can be ascribed to the formation of B_4C (ICDD PDF card #35–0789) due to the reaction of the nanoparticles and graphite crucible during the borothermal reduction process at the relatively high temperature. Apart from these, no other peaks, such as those attributable to hafnium oxides and boron oxides, are detected.

The morphology and microstructure of the HfB_2 nanoparticles are investigated by SEM and TEM. Fig. 2(a and b) show the SEM images of the prepared HfB_2 nanoparticles at different magnifications. It can be seen that the nanoparticles exhibits a porous structure, composed of irregular HfB_2 particles with sizes ranging from ~100 nm to ~1 μm. Fig. 2(c and d) show the TEM images of HfB_2 nanoparticles recorded at two different positions. It can be observed that there are some small round particles with diameters of around 180 nm and some rod-like particles with larger sizes. Since there is a high-temperature sintering step in the synthesis process of HfB_2 nanoparticles, some small particles

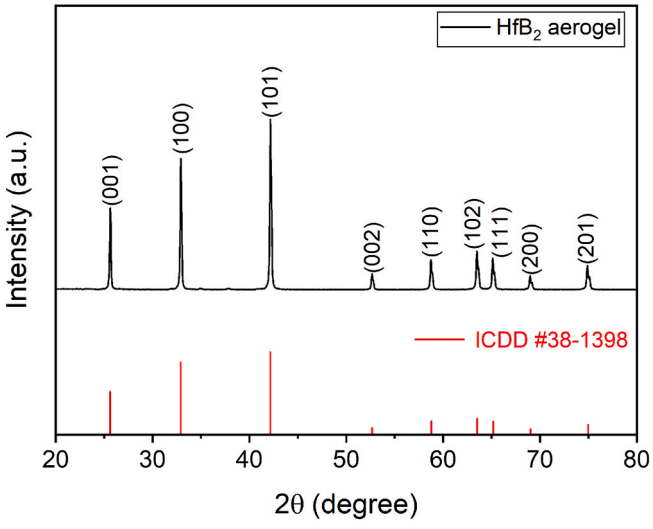

Fig. 1. XRD pattern of the prepared HfB_2 nanoparticles.

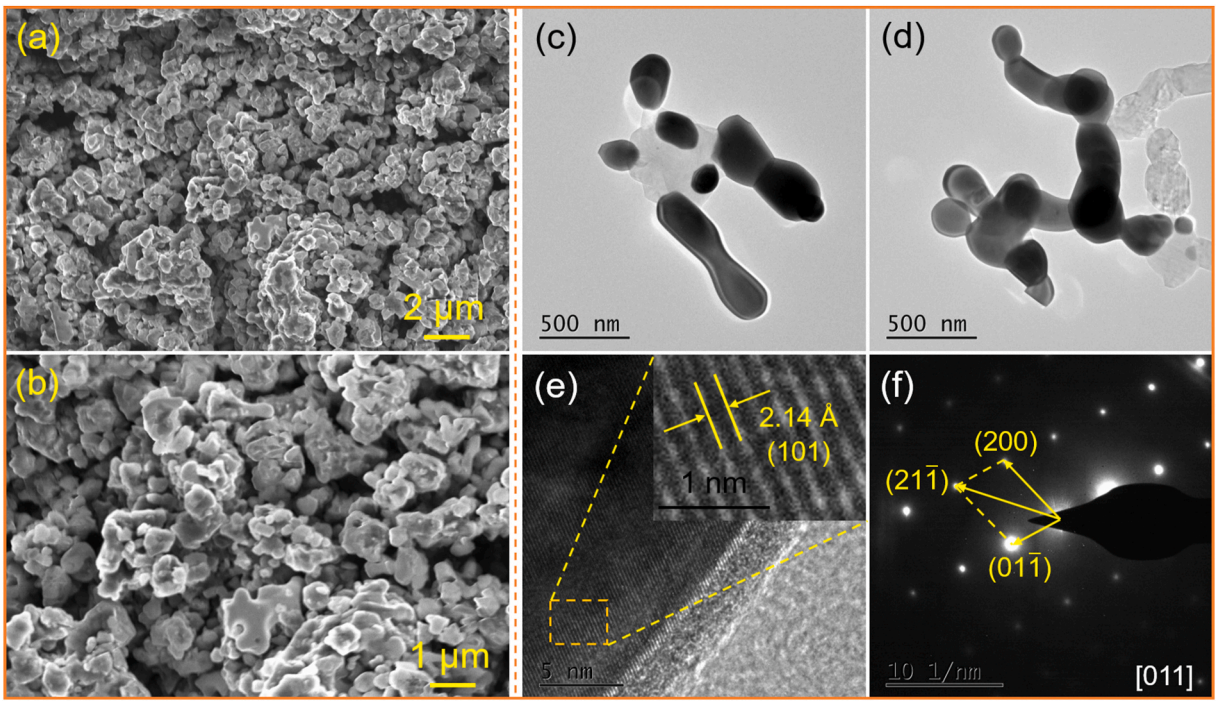

Fig. 2. (a) Low and (b) high-magnification FESEM images of HfB_2 nanoparticles; (c, d) TEM and (e) HRTEM images of HfB_2 nanoparticles, (f) the corresponding SEAD pattern.

may fuse together to form the larger particles. The HRTEM image is presented in Fig. 2(c), where the well-defined lattice fringes can be clearly observed. The measured spacing between two adjacent lines is 2.14 Å, which matches well with the *d*-spacing of (101) planes of hexagonal HfB_2 [31]. The corresponding SEAD pattern in Fig. 2(d) shows a clear spot array, demonstrating that the HfB_2 particles are of single crystal structure.

X-ray photoelectron spectroscopy is conducted to probe the surface

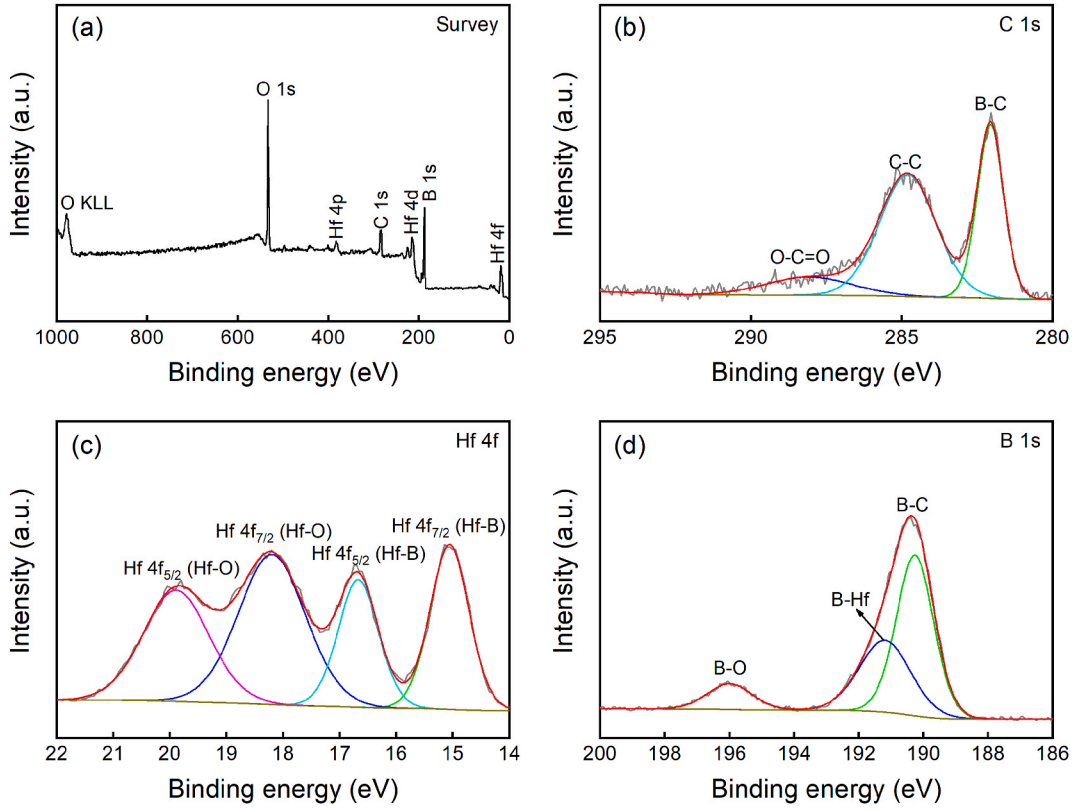

Fig. 3. XPS characterization results of HfB_2 nanoparticles: (a) survey scan spectrum; (b) C 1s region with peak fitting; (c) Hf 4f region with peak fitting; (d) B 1s region with peak fitting.

composition and chemical state of the prepared HfB_2 nanoparticles. The survey scan spectrum is shown in Fig. 3(a). In addition to the C 1s peak commonly detected due to the adventitious carbon from the contamination in air, a relatively strong O 1s peak is also observed. To further investigate the surface composition of the as-synthesized HfB_2 nanoparticles, the high-resolution spectra of C 1s, Hf 4f, and B 1s regions are recorded. As can be seen in Fig. 3(b), the C 1s peak is deconvoluted into three components. The middle peak at 284.8 eV can be assigned to C–C bond, which is also used as the reference for charge calibration of all the XPS spectra [32]. The peak at lower binding energy of 282.07 eV is attributed to C–B bonding [33,34]; this reveals the existence of B_4C on the surface of the prepared HfB_2 nanoparticles, which is in agreement with the appearance of faith B_4C peaks in the XRD pattern. The smaller peak at 288.07 eV is well accepted to correspond to the O–C═O bonding caused by adventitious carbon [35,36]. Fig. 3(c) shows the Hf 4f region of the spectrum, where two Hf bonding environments are observed. The peaks located at 15.06 and 16.67 eV are referred to $Hf_{7/2}$ and $Hf_{5/2}$ doublet of HfB_2, respectively, while the peaks located at 18.20 and 19.89 eV are attributed to $Hf_{7/2}$ and $Hf_{5/2}$ of HfO_2, respectively [37]. Furthermore, the B 1s region spectrum together with the deconvoluting and fitting results are shown in Fig. 3(d) and indicate the existence of three B components. The peaks at 187.51 and 188.44 eV correspond to B–C and B–Hf bonding environments that come from B_4C and HfB_2, respectively [38,39]. In addition, the peak at 193.25 eV matches with the characteristic XPS peak of B–O bond [40], which may be induced by the residual B_2O_3 in the HfB_2 nanoparticles. In summary, the XPS results confirm that the HfB_2 has been successfully synthesized, but with the presence of HfO_2, B_2O_3, B_4C in the near surface region of the particles comprising the as-synthesized HfB_2 nanoparticles. The presence of B_4C can also be evidenced in the XRD result; however, no characteristic peaks of HfO_2 and B_2O_3 can be observed in the XRD pattern, which indicates that the HfO_2 and B_2O_3 could be amorphous in nature or crystallized but present in a relatively low amounts.

3.2. Gas sensing properties

Fig. 4 shows the responses and the corresponding dynamic response and recovery curves of the sensor to 10 ppm NO_2 at different operating temperatures. It can be seen in Fig. 4(a) that the response decreases with increasing operating temperature, namely, a higher NO_2 response is observed at a lower operating temperature. However, as shown in Fig. 4 (b and c), the response times at 100 and 150 °C are rather long and the sensor cannot fully recover to its initial resistance even after 10 min. This can be due to the slow desorption rate of NO_2 from the surface of the HfB_2 sensing layer at low operating temperatures. When the operating temperature is raised to 200 °C, the sensor shows good response and recovery characteristics to NO_2 and can fully recover after the NO_2 purge. Considering that the good reversibility, which ensures the continuous sensing capability, is one of the fundamental parameters of a gas sensor, in this study 200 °C is selected as the optimum operating temperature of the sensor for further gas sensing tests.

The transient response of the sensor to varied concentrations of NO_2 at the operating temperature of 200 °C is shown in Fig. 5(a). The sensor resistance drops quickly upon exposure to NO_2. If the charge transfer is considered as the basic mechanism for the sensor resistance change, the result suggests that NO_2 molecules can trap/inject electrons from/to the HfB_2 during their interaction. Such a sensing behavior is similar to that of the *p*-type semiconducting metal oxide gas sensing materials. When turning off the NO_2 flow, the sensor resistance recovers to its initial value, indicating good reversibility of the HfB_2 nanoparticles-based sensor. In addition, it can be seen that the resistance changes of the sensor to identical concentrations of NO_2 are almost the same. Namely, the sensor shows a constant response to a specific NO_2 concentration. This suggests that the sensor has a good reproducibility. Furthermore, a discernible response of 1% to 0.1 ppm NO_2 can be clearly observed in this figure, which indicates a low NO_2 detection limit of the sensor. Closer analysis of the sensor response vs. the NO_2 concentration is shown in Fig. 5(b). The sensor response increases from 1% to 28% with increasing NO_2 concentration from 0.1 to 10 ppm and their relationship can be fitted using the expression $y = 9.593x^{0.475}$ (the standard errors for y and x are 0.684 and 0.038, respectively), where y is the sensor response (%) and x is the NO_2 concentration in ppm.

The dynamic response and recovery curves of the sensor to 10 ppm NO_2 in Fig. 6(a) confirm good reversibility and reproducibility of the sensor. To further evaluate the sensor stability, the reversible NO_2 sensing cycles are tested and recorded over a period of 24 days, the

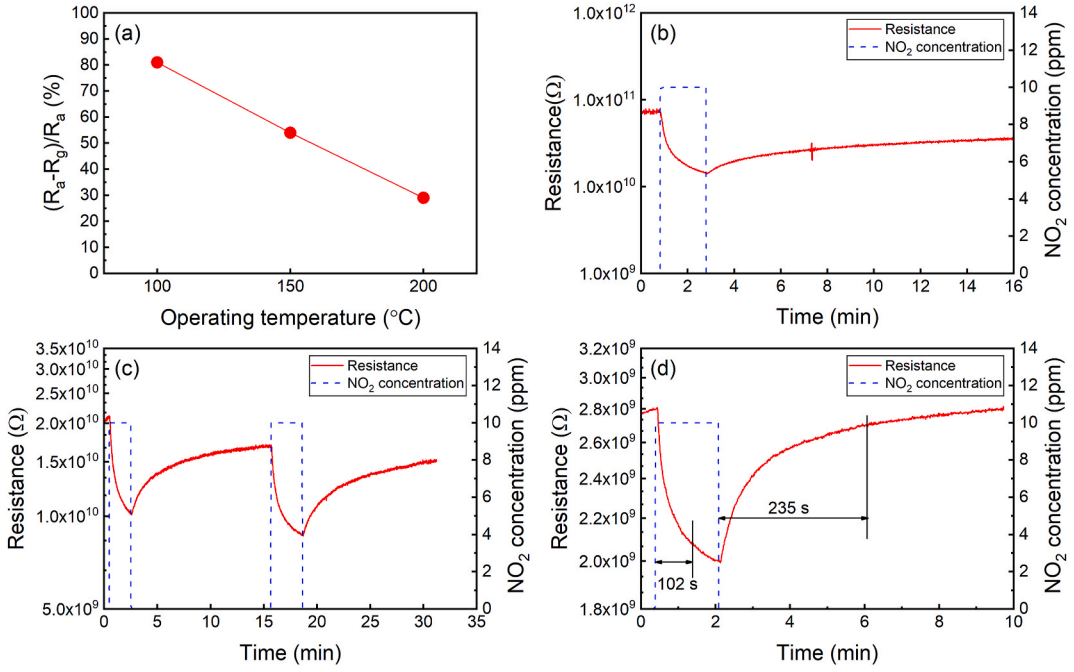

Fig. 4. (a) Responses of the sensor to 10 ppm NO_2 at different operating temperatures; (b), (c), and (d) are the dynamic response and recovery curves of the sensor upon exposure to 10 ppm NO_2 at the operating temperature of 100, 150, 200 °C, respectively.

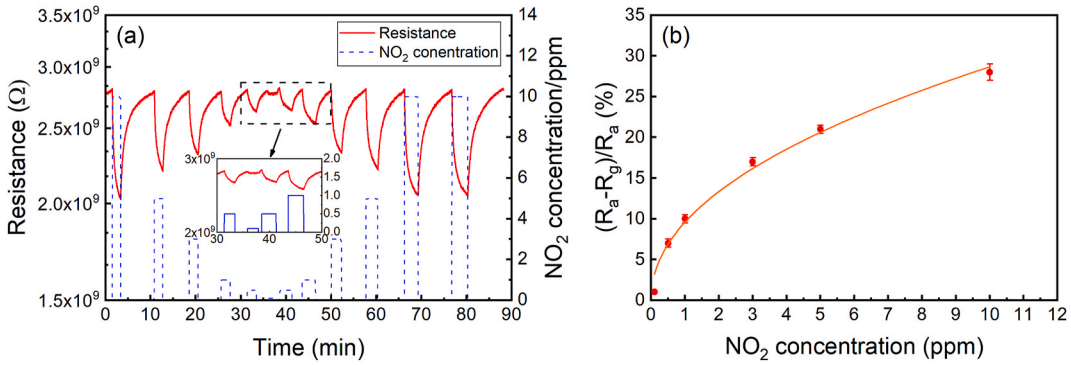

Fig. 5. (a) Dynamic response and recovery curves and (b) responses of HfB_2 to different concentrations of NO_2 at 200 °C.

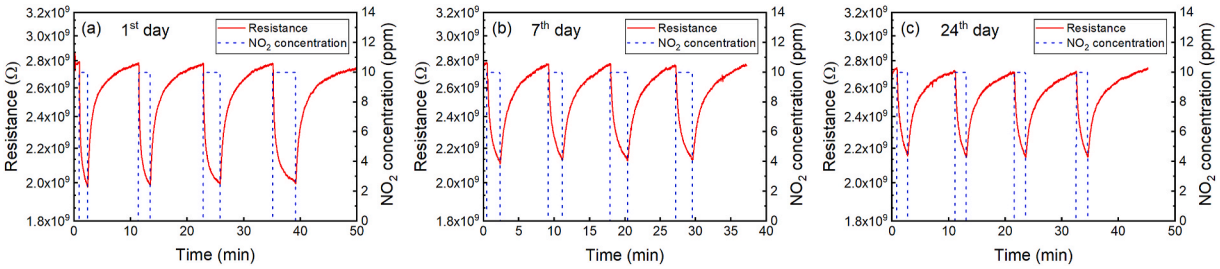

Fig. 6. Dynamic response and recovery curves to 10 ppm NO_2 at the operating temperature of 200 °C. (a), (b), and (c) are the results recorded at the 1st, 7th, and 24th day of testing.

results of which are shown in Fig. 6(b and c). Comparing the data recorded at the 1st, 7th, and 24th days, the sensor shows good and consistent response and recovery characteristics over this period. The sensor response reduces from 28% to 21.5% after one week but retains this value during the rest of the examined time. Overall, the HfB_2 nanoparticles-based sensor has a good stability for NO_2 sensing, which is as expected due to the chemical and thermal stability of HfB_2.

The cross-sensitivity of the sensor to NO_2 was assessed by separately exposing the sensor to ammonia (NH_3), ethanol (C_2H_5OH), formaldehyde (CH_2O), acetone (C_3H_6O), and carbon dioxide (CO_2) of a comparable or higher concentration. All the tests were carried out at the operating temperature of 200 °C and the results are presented in Fig. 7.

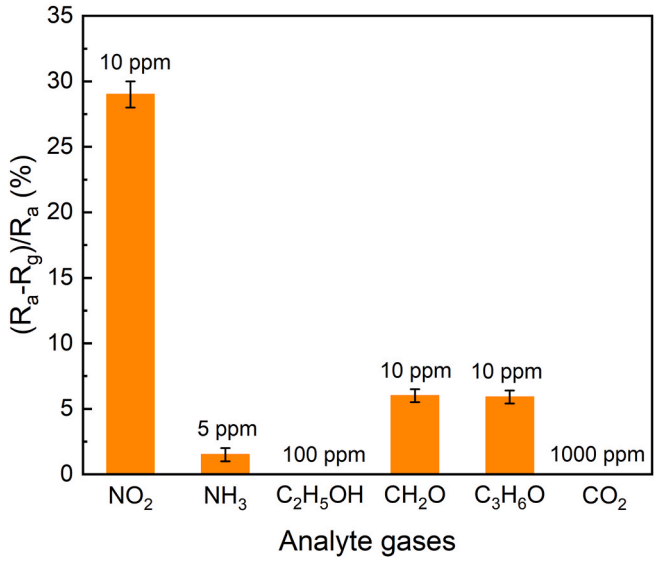

Fig. 7. Responses of HfB_2 to different gases at the operating temperature of 200 °C.

The sensor shows no discernible response to 100 ppm C_2H_5OH and 1000 ppm CO_2, while responses of 1.3%, 6.0%, 5.9% are observed for 5 ppm NH_3, 10 ppm CH_2O, and 10 ppm C_3H_6O, respectively, which are much lower than that to NO_2 under similar concentrations, indicating a good selectivity of the sensor to NO_2.

Fig. S4 shows the dynamic response and recovery curves of the sensor to NH_3, CH_2O, and C_3H_6O. It can be seen that, similar to NO_2, the sensor resistance decreases upon exposure to all these gases. This phenomenon is different from the conductometric gas sensors based on metal oxide semiconductors, for which the gas sensing mechanism generally involves the redox reaction between the test gases and the oxygen species that adsorbed on the surface of the sensing materials. Briefly, when the sensor is in air, oxygen molecules are chemisorbed on the surface of the metal oxides to form O_2^-, O^- , and O^{2-}, depending on the temperature [41]. These adsorbed oxygen species can then react with the target gases, resulting in electron transfer between the test gas and the metal oxide gas sensing materials and, consequently, in a resistance change (sensing signal) of the sensor [42]. Under this mechanism, NO_2 is usually considered as an oxidizing gas while NH_3, CH_2O, and C_3H_6O are considered as reducing gases, and the resistance change of the metal oxides-based sensors follow opposite directions upon exposure to these two different types of gases. This suggests that HfB_2 follows a different gas sensing mechanism from the widely investigated conductometric gas sensing materials of metal oxides. Furthermore, as discussed above, the oxygen molecules play a bridge-role in the gas sensing process of metal oxides. To provide further insight, we have compared the sensor responses towards NO_2, NH_3, CH_2O, and C_3H_6O in air and in N_2, as shown in Fig. S5. It is found that the sensor response to these gases in air and N_2 is nearly identical. Namely, the sensor response of HfB_2 is essentially independent of the oxygen molecules, which further suggests a gas sensing mechanism different from metal oxides.

As pointed out by some reports [43,44], for metal oxide semiconductors, oxygen species are mainly adsorbed on oxygen vacancies, which then react with the target gases and act as a bridge for electron transfer between the sensing materials and the target gases. This is considered the reason why metal oxide-based sensors show opposite

resistance changes upon exposure to reducing and oxidizing gases and why higher responses are usually observed in materials with more oxygen vacancies [45,46]. Here, for HfB_2, we speculate that the adsorption of the tested gases on the surface of the HfB_2 nanoparticles is dominantly a physical process due to the lack of the surface chemisorbed oxygen, leading to the same resistance variation trend (decrease) upon exposure to all the tested gases and the observed independence on oxygen concentration. One evidence to support this conclusion is the similar resistance values of the sensor in air and in N_2 (see Fig. S6), in contrast to the significant difference in baseline resistance in N_2 and air observed for metal oxides due to oxygen in air trapping electrons from the conduction band of the metal oxides [47,48]. However, in order to fully understand this, much more work needs to be carried out. Nevertheless, the results show that HfB_2 and potentially other transition metal diborides may provide a new material library for conductometric gas sensing applications.

4. Conclusion

In this study, the gas sensing properties of HfB_2 nanoparticles were investigated using an interdigitated Ag/Pd gas sensing electrode. The HfB_2 nanoparticles was prepared by a sol-gel method followed by ambient drying and borothermal reduction processes. The as-synthesized HfB_2 nanoparticles was composed of HfB_2 particles and showed a porous structure. The operating temperature of 200 °C was selected as the operating temperature of the sensor for NO_2 sensing, when considering both the response and response/recovery time. Under this condition, the sensor showed good reversibility, reproducibility, stability, and selectivity to NO_2. Furthermore, it was observed that the sensor exhibited a reduced resistance state in response to both oxidizing and reducing gases and showed a near identical response to the tested gases in both N_2 and air background. Such phenomena are distinct from those observed in studies of metal oxide gas sensing materials; thus, HfB_2 may possess a different gas sensing mechanism from the metal oxides, warranting further fundamental investigation.

Declaration of competing interest

The authors declare that they have no known competing financial interests or personal relationships that could have appeared to influence the work reported in this paper.

Acknowledgements

The project was supported by U.S. National Science Foundation (grant # 1903188) and the Industrial Members of the Berkeley Sensor & Actuator Center. Work at the Molecular Foundry was supported by the Office of Science, Office of Basic Energy Sciences, of the U.S. Department of Energy under Contract No. DE-AC02-05CH11231. SZ, YX and ZL would like to acknowledge additional support by the China Scholarship Council.

Appendix A. Supplementary data

Supplementary data to this article can be found online at https://doi.org/10.1016/j.ceramint.2021.11.235.

References

[1] T. Seiyama, A. Kato, K. Fujisishi, M. Nagatoni, A new detector for gaseous components using semiconductive thin films, Anal. Chem. 34 (1962) 1052–1053.
[2] S.R. Morrison, Semiconductor gas sensors, Sensor. Actuator. 2 (1990) 329–341.
[3] T. Naoyoshi, Gas-detecting Device, US, 1971.
[4] E. Comini, Metal oxide nano-crystals for gas sensing, Anal. Chim. Acta 568 (2005) 28–40.
[5] S. Zhao, Y. Shen, P. Zhou, F. Hao, Y. Shen, Enhanced NO_2 sensing performance of ZnO nanowires functionalized with ultra-fine In_2O_3 nanoparticles, Sensor. Actuator. B Chem. 308 (2020) 127729.
[6] H. Long, A. Harley-Trochimczyk, T. Pham, Z. Tang, T. Shi, A. Zettl, et al., High surface area MoS2/graphene hybrid aerogel for ultrasensitive NO_2 detection, Adv. Funct. Mater. 26 (2016) 5158–5165.
[7] S.A. Ak Ba R, D.R. Miller, P.A. Morris, Nanoscale metal oxide-based heterojunctions for gas sensing: a review, Sensor. Actuator. B Chem. 204 (2014) 250–272.
[8] Y.F. Sun, S.B. Liu, F.L. Meng, J.Y. Liu, J.H. Liu, Metal oxide nanostructures and their gas sensing properties: a review, Sensors 12 (2012) 2610–2631.
[9] R. Chen, J. Wang, Y. Xia, L. Xiang, Near infrared light enhanced room-temperature NO_2 gas sensing by hierarchical ZnO nanorods functionalized with PbS quantum dots, Sensor. Actuator. B Chem. 255 (2017) 2538–2545.
[10] Y. Shen, X. Chen, W. Wang, Y. Gong, S. Chen, J. Liu, et al., Complexing surfactants-mediated hydrothermal synthesis of WO_3 microspheres for gas sensing applications, Mater. Lett. 163 (2016) 150–153.
[11] T. Yamazaki, C. Jin, Y. Shen, T. Kikuta, N. Nakatatani, Microstructure and gas sensing property of porous SnO_2 sputtered films, Mater. Sci. Forum 539 (2007) 3508–3513.
[12] S. Zhao, Y. Shen, P. Zhou, J. Zhang, W. Zhang, X. Chen, et al., Highly selective NO_2 sensor based on p-type nanocrystalline NiO thin films prepared by solgel dip coating, Ceram. Int. 44 (2018) 753–759.
[13] S. Zhao, Y. Shen, P. Zhou, X. Zhong, C. Han, Q. Zhao, et al., Design of Au@WO_3 core−shell structured nanospheres for ppb-level NO_2 sensing, Sensor. Actuator. B Chem. 282 (2019) 917–926.
[14] W. Yan, A. Harley-Trochimczyk, L. Hu, L. Chen, R. Maboudian, Conductometric gas sensing behavior of WS_2 aerogel, FlatChem 5 (2017) 1–8.
[15] L. Min, D. Zhou, J. Zhao, Z. Zheng, J. He, H. Long, et al., Resistive gas sensors based on colloidal quantum dot (CQD) solids for hydrogen sulfide detection, Sensor. Actuator. B Chem. 217 (2015) 198–201.
[16] R. Xing, Y. Xue, X. Liu, B. Liu, B. Miao, W. Kang, et al., Mesoporous ZnS hierarchical nanostructures: facile synthesis, growth mechanism and application in gas sensing, CrystEngComm 14 (2012) 8044–8048.
[17] D.W. Gardner, X. Gao, H.M. Fahad, A.T. Yang, S. He, A. Javey, et al., Transistor-based work-function measurement of metal-organic frameworks for ultra-low-power, rationally designed chemical sensors, Chemistry 57 (2019) 13176–13183.
[18] K.R. Nemade, S.A. Waghuley, Chemiresistive gas sensing by few-layered graphene, J. Electron. Mater. 42 (2013) 2857–2866.
[19] Z. Song, Z. Wei, B. Wang, L. Zhen, H. Liu, Sensitive room-temperature H_2S Gas sensors employing SnO_2 quantum wire/reduced graphene oxide nanocomposites, Chem. Mater. 28 (2016) 1205–1212.
[20] H. Long, L. Chan, A. Harley-Trochimczyk, L.E. Luna, Z. Tang, T. Shi, et al., 3D MoS_2 aerogel for ultrasensitive NO_2 detection and its tunable sensing behavior, Adv. Mater. Interfac. 16 (2017) 1700217.
[21] D. Sarkar, X. Xie, J. Kang, H. Zhang, W. Liu, J. Navarrete, et al., Functionalization of transition metal dichalcogenides with metallic nanoparticles: implications for doping and gas-sensing, Nano Lett. 15 (2015) 2852–2862.
[22] J. Bing Hwang, A microscopic gas-sensing model for ethanol sensors based on conductive polymer composites from polypyrrole and poly (ethylene oxide), J. Electrochem. Soc. 146 (1999) 1231.
[23] C. Pandis, V. Peoglos, A. Kyritsis, P. Pissis, Gas sensing properties of conductive polymer nanocomposites, Procedia Eng. 25 (2011) 243–246.
[24] H.L. Sang, W. Eom, H.S. Shin, R.B. Ambade, T.H. Han, Room-temperature, highly durable $Ti_3C_2T_x$ MXene/graphene hybrid fibers for NH_3 gas sensing, ACS Appl. Mater. Interfaces 12 (2020) 10434–10442.
[25] E. Lee, A. Vahidmohammadi, B.C. Prorok, Y.S. Yoon, M. Beidaghi, D.J. Kim, Room temperature gas-sensing of two-dimensional titanium carbide (MXene), ACS Appl. Mater. Interfaces 9 (2017) 37184–37190.
[26] J. Zhang, S. Xiong, J. Wang, Y. Ni, C. Ke, Silicothermic synthesis of phase-pure HfB_2 fine powder, J. Am. Ceram. Soc. 104 (2021) 785–792.
[27] J.W. Lawson, C.W. Bauschlicher, M.S. Daw, Ab initio computations of electronic, mechanical, and thermal properties of ZrB_2 and HfB_2, J. Am. Ceram. Soc. 94 (2011) 3494–3499.
[28] J.T. Cahill, S. Turner, J. Ye, B. Shevitski, M.A. Worsley, Ultrahigh-temperature ceramic aerogels, Chem. Mater. 31 (2019) 3700–3704.
[29] C. Musa, R. Licheri, R. Orru, G. Cao, A. Balbo, F. Zanotto, et al., Optical characterization of hafnium boride and hafnium carbide-based ceramics for solar energy receivers, Sol. Energy 169 (2018) 111–119.
[30] Z. Liu, P. Wang, Q. Cui, G. Yang, S. Jin, K. Xiong, Theoretical prediction of HfB_2 monolayer, a two-dimensional Dirac cone material with remarkable Fermi velocity, RSC Adv. 9 (2019) 2740–2745.
[31] X. Ren, H. Mo, W. Wang, P. Feng, L. Guo, Z. Li, Ultrahigh temperature ceramic HfB_2-SiC coating by liquid phase sintering method to protect carbon materials from oxidation, Mater. Chem. Phys. 217 (2018) 504–512.
[32] R.P. Vasquez, R.A. Brain, D. Ross, N.C. Yeh, Epitaxial C60 film on Si (111) by XPS, Surf. Sci. Spectra 1 (1992) 242–245.
[33] T. Hu, L. Steihl, W. Rafaniello, T. Fawcett, D.D. Hawn, J.G. Mashall, et al., Structures and properties of disordered boron carbide coatings generated by magnetron sputtering, Thin Solid Films 332 (1998) 80–86.
[34] H. Wang, Q. Guo, J. Yang, Y. Zhao, X. Wang, Z. Tao, et al., Microstructure and thermophysical properties of B_4C/graphite composites containing substitutional boron, Carbon 52 (2013) 10–16.
[35] L. Shi, Y. Gu, L. Chen, Y. Qian, Z. Yang, J. Ma, A low temperature synthesis of crystalline B_4C ultrafine powders, Solid State Commun. 128 (2003) 5–7.
[36] Y. Zhang, Y. Wang, C. Han, S. Jia, S. Zhou, J. Zang, Tungsten-coated nano-boron carbide as a non-noble metal bifunctional electrocatalyst for oxygen evolution and hydrogen evolution reactions in alkaline media, Nanoscale 9 (2017) 19176–19182.

[37] A.S. Sokolov, Y.-R. Jeon, S. Kim, B. Ku, D. Lim, H. Han, et al., Influence of oxygen vacancies in ALD HfO_{2-x} thin films on non-volatile resistive switching phenomena with a $Ti/HfO_{2-x}/Pt$ structure, Appl. Surf. Sci. 434 (2018) 822–830.
[38] L. Chen, T. Goto, T. Hirai, T. Amano, State of boron in chemical vapour-deposited SiC-B composite powders, J. Mater. Sci. Lett. 9 (1990) 997–999.
[39] G. Mavel, J. Escard, P. Costa, J. Castaing, ESCA surface study of metal borides, Surf. Sci. 35 (1973) 109–116.
[40] V.I. Nefedov, D. Gati, B.F. Dzhurinskii, N.P. Sergushin, Y.V. Salyn, X-ray electron study of oxides of elements, Zh. Neorg. Khim. 20 (1975) 2307–2314.
[41] S. Zhao, Y. Shen, F. Hao, C. Kang, B. Cui, D. Wei, et al., P-n junctions based on CuO-decorated ZnO nanowires for ethanol sensing application, Appl. Surf. Sci. 538 (2021) 148140.
[42] P. Shankar, J.B.B. Rayappan, Gas sensing mechanism of metal oxides: the role of ambient atmosphere, type of semiconductor and gases-a review, Sci. Lett. J. 4 (2015) 126.
[43] D. Degler, U. Weimar, N. Barsan, Current Understanding of the fundamental mechanisms of doped and loaded semiconducting metal-oxide-based gas sensing materials, ACS Sens. 4 (2019) 2228–22249.
[44] Z. Wang, J. Xue, D. Han, F. Gu, Controllable defect redistribution of ZnO nanopyramids with exposed {1011} facets for enhanced gas sensing performance, ACS Appl. Mater. Interfaces 7 (2015) 308–317.
[45] C. Mei, Z. Wang, D. Han, F. Gu, G. Guo, Porous ZnO polygonal nanoflakes: synthesis, use in high-sensitivity NO_2 gas sensor, and proposed mechanism of gas sensing, J. Phys. Chem. C 115 (2011) 12763–12773.
[46] M. Al-Hashem, S. Akbar, P. Morris, Role of oxygen vacancies in nanostructured metal-oxide gas sensors: a review, Sensor. Actuator. B Chem. 301 (2019) 126845.
[47] H. Colak, E. Karakose, Synthesis and characterization of different dopant (Ge, Nd, W)-doped ZnO nanorods and their CO_2 gas sensing applications, Sensor. Actuator. B Chem. 296 (2019) 126629.
[48] H. Nguyen, S.A. El-Safty, Meso-and macroporous Co_3O_4 nanorods for effective VOC gas sensors, J. Phys. Chem. C 115 (2011) 8466–8474.